Naval Research Laboratory

Washington, DC 20375-5320

NRL/MR/7322--19-9953

Development and Testing of a Rogue Wave Threat Estimator for WAVEWATCH III®

MarkD. Orzech
Julian Simeonov
Michail Manolidis

Ocean Dynamics & Prediction Branch
Oceanography Division

November 13, 2019

REPORT DOCUMENTATION PAGE

Form Approved
OMB No. 0704-0188

1. REPORT DATE *(DD-MM-YYYY)*	**2. REPORT TYPE**	**3. DATES COVERED** *(From - To)*
13-11-2019	NRL Memorandum Report	01 Oct 2016 – 25 Sept 2019

4. TITLE AND SUBTITLE

Development and Testing of a Rogue Wave Threat Estimator for WAVEWATCH III®

5a. CONTRACT NUMBER

5b. GRANT NUMBER

5c. PROGRAM ELEMENT NUMBER

6. AUTHOR(S)

Mark D. Orzech, Julian Simeonov, and Michail Manolidis

5d. PROJECT NUMBER

5e. TASK NUMBER

5f. WORK UNIT NUMBER
6A51

7. PERFORMING ORGANIZATION NAME(S) AND ADDRESS(ES)

Naval Research Laboratory
1009 Balch Blvd
Stennis Space Center, MS 39529-5004

8. PERFORMING ORGANIZATION REPORT NUMBER

NRL/MR/7322--19-9953

9. SPONSORING / MONITORING AGENCY NAME(S) AND ADDRESS(ES)

Office of Naval Research
One Liberty Center
875 N. Randolph Street, Suite 1425
Arlington, VA 22203-1995

10. SPONSOR / MONITOR'S ACRONYM(S)

ONR

11. SPONSOR / MONITOR'S REPORT NUMBER(S)

12. DISTRIBUTION / AVAILABILITY STATEMENT

DISTRIBUTION STATEMENT A: Approve for public release; distribution is unlimited.

13. SUPPLEMENTARY NOTES

14. ABSTRACT

This report describes the development and implementation of a post-processing utility in the phase-averaged model for wind-generated surface gravity waves, WAVEWATCH III®. The utility estimates the relative likelihood of rogue wave development based on four contributing factors: spectral frequency modulation, adverse current gradients, directional distribution of waves, and wind forcing. A simple scalar estimate of this type has not previously been available in this model, although an estimation of space-time extreme waves based on statistical calculations from wave spectra has been implemented (Barbariol et al., 2017). Preliminary rogue threat maps from the prototype utility are presented, and limited testing is conducted to examine variations in model output for confirmed rogue versus non-rogue events. Potential future improvements to incorporate additional causal factors, such as shallow-water bathymetry, into the utility are discussed.

15. SUBJECT TERMS

Rogue waves WAVEWATCH
Rogue threat index Modulational instability

16. SECURITY CLASSIFICATION OF:			**17. LIMITATION OF ABSTRACT**	**18. NUMBER OF PAGES**	**19a. NAME OF RESPONSIBLE PERSON**
a. REPORT	**b. ABSTRACT**	**c. THIS PAGE**			Mark D. Orzech
Unclassified Unlimited	Unclassified Unlimited	Unclassified Unlimited	Unclassified Unlimited	32	**19b. TELEPHONE NUMBER** *(include area code)* (228) 688-5974

Standard Form 298 (Rev. 8-98)
Prescribed by ANSI Std. Z39.18

This page intentionally left blank.

Contents

List of Figures

1 INTRODUCTION

This report documents progress in the implementation of a utility to estimate the relative likelihood of anomalously large, or ***rogue***, waves in the WAVEWATCH III® ("WW3") model. WW3 was originally developed at Delft University (Tolman 1991), but in its current form, it is maintained in a repository at NOAA's NCEP (Tolman et al. 2002). At time of writing, the last public release of WW3 was WW3 version 6.07 (WW3 Development Group 2019, henceforth "WW3DG 2019"), and a succeeding version is under active development via a Subversion (svn) software versioning and revision control system administered by NCEP. As of March 2019, WW3DG has shifted to an open development paradigm in which the latest software release package may be accessed and/or modified at the following GitHub site: https://github.com/NOAA-EMC/WW3/releases/tag/6.07.1.

The governing equation of WW3 is the action balance equation, based on the evolution of the action density, N (i.e., energy density, E, normalized by angular frequency, σ). In simplified form, it may be expressed as:

$$\frac{\partial N}{\partial t}+\frac{\partial C_x N}{\partial x}+\frac{\partial C_y N}{\partial y}+\frac{\partial C_\sigma N}{\partial \sigma}+\frac{\partial C_\theta N}{\partial \theta}=\frac{S}{\sigma} \tag{1}$$

The action density is a function of location, frequency, direction, and time: $N = N(x, y, \sigma, \theta, t)$. Relative wave frequency σ is measured from a frame of reference moving with any existing current, and θ is wave direction. C is the wave action propagation speed in both geographic and spectral space, with subscripts indicating the component of group velocity (C_g) in the x, y, σ, and θ axis directions. The right hand side of (1) is the sum of all source/sink terms normalized by frequency, $S = S(x, y, \theta, \sigma, t)$. In more recent versions of WW3, this sum includes $S_{in} + S_{nl} + S_{ds} + S_{ice}$; i.e., input by wind, nonlinear interactions, dissipation, and wave-ice interactions, respectively. The rogue threat utility will perform post-processing computations using N and other separate field parameters; it does not require modification of any components of (1).

Anomalously large – or "rogue" – waves are most commonly defined as those with wave height $H_r > 2{\cdot}H_s$ or crest height $\eta_r > 1.25{\cdot}H_s$, where H_s is the concurrent significant wave height in the local region. Rogues can be produced by a range of both linear and nonlinear interactions, and they may occur under any given sea state. Commonly used theoretical wave height distributions such as the Rayleigh distribution generally place rogue wave heights along their far right side where probability is very low; thus, if we take such distributions to be fully representative of the true ocean state we should correspondingly expect rogue waves to be very rare.

Although they indeed appear to be relatively uncommon in the deep water ocean, large rogues are not so rare that they are never encountered by oceangoing vessels or structures. When they are encountered, such unexpected extreme waves can be very destructive and dangerous. An extensive 40-year survey by Liu (2007) found that roughly one large ship or platform per year was reported to be seriously damaged or destroyed by rogue waves. There have also been numerous recorded incidents involving U.S. Naval vessels, each resulting in varying degrees of damage, injury, and mission delays (e.g., *https://www.navysite.de*).

Over the past several decades, theoretical, numerical, and experimental investigations have identified various environmental conditions under which rogue wave likelihood appears to increase (e.g., Babanin & Rogers, 2014; Kharif et al., 2009). The fundamental physical mechanism upon which the present study and the resulting rogue threat utility will rely is wave

Manuscript approved September 26, 2019.

growth produced by the **modulational instability** of nonlinear wave fields (Zakharov, 1967; Benjamin & Feir, 1967; McLean, 1982). This nonlinear process is different from the simpler linear superposition of overlapping wave fronts and can result in rapid wave height increases in a relatively short time (Chalikov, 2009). It will be described in greater detail in Section 3.1.1.

The modulational instability can be facilitated or hampered by specific environmental factors, under particular conditions. When a wave train is opposed by a **current gradient**, in which current magnitude increases as the waves propagate forward, nonlinearity of the wave field can grow more rapidly (Manolidis et al., 2019). If the **directional distribution** of a given wave spectrum is very broad, rogue wave likelihood can drop (e.g., Onorato et al., 2009). If a spectrum is directionally bimodal (i.e., "crossing seas" with wave fronts converging from two separate directions), it can result in larger wave heights through linear superposition, but it will also tend to reduce the rate of nonlinear wave growth (although there are localized variations at specific bimodal angles; e.g., Gramstad et al., 2018). And while moderate winds blowing in the same direction as a wave train can increase its nonlinearity, **stronger winds** can potentially "overload" the high frequency components of the wave spectrum and produce wave breaking that also limits or reverses rogue wave growth (Galchenko et al., 2012; Babanin et al., 2010). At present, operational WW3 forecasts do not consider the potential effects of these environmental conditions on the likelihood of rogue waves.

To address this operational gap, we have developed a rogue threat estimation utility that is being integrated into the WW3 forecasting system. In this report, we describe the theory, numerical implementation, and preliminary testing of the utility, which computes the relative likelihood of rogue wave events in deep water due to the four environmental causal factors identified above (i.e., modulational instability, adverse current gradients, wave directional distribution, and wind effects). The system utilizes WW3 spectra in combination with user-supplied datasets on ocean surface currents and atmospheric winds. As wave spectra such as those produced by WW3 are stochastic, representing time-averaged conditions, they are not suited to the prediction of individual rogue waves at specific times. In lieu of this, our spectrally based approach computes a scalar *rogue threat index* (**RTI**) whose magnitude indicates the risk that a rogue event will occur sometime within the timeframe described by the selected wave spectrum.

A statistical estimation of extreme wave likelihood has been implemented previously in WW3 using a statistical Euler Characteristics (EC) approach (Babariol et al., 2017; also WW3DG 2019, Section 3.11). This method computes the probability of exceedance of the maximal sea surface elevation as the mean value of the EC (Fedele et al., 2012). Space-time extreme wave heights are estimated at each grid location using a Quasi-Determinism model to predict the mean shape of the wave group near the apex of its development (Fedele 2012; Benetazzo et al., 2015). This method does not consider nonlinear contributions from environmental factors such as currents or winds, relying instead on probabilistic computations of wave height ranges under given spectral conditions.

This report will describe the theory, implementation, and initial testing of a new rogue threat estimation utility for WW3 that does consider the role played by four specific environmental factors. The general structure and conventions of the WW3 code are described in Section 2. The rogue threat index and its components are described in greater detail in Section 3, with theoretical background provided in Section 3.1 and the numerical implementation of each causal factor component detailed in Section 3.2. Section 4 presents sample output from the prototype

utility and describes preliminary evaluation and validation testing conducted with WW3 datasets. Conclusions and plans for further work are discussed in Section 5.

2 WW3 CODE: INPUT REQUIREMENTS

We are currently in the process of fully integrating the rogue threat utility into the WW3 system. As the rogue wave threat index computation will be performed as part of model post-processing, it will not require new types of input files or new parameters beyond those already available in WW3. However, because the utility relies on ocean current and wind fields, the model must be instructed to read in these fields, and the user must provide the necessary input specification files (e.g., *ww3_prep_current.inp* and *ww3_prep_wind.inp*) in one of the accepted formats (see WW3DG 2019). To activate the rogue index computation, an additional specifier string (not yet set; most likely to be "RTI") will need to be included in the input "switch" file. This will enable the loading of current and wind data by WW3. If the computation of current and/or wind effects on wave propagation is not otherwise activated, the RTI switch will limit WW3 to loading and gridding these data as part of its preprocessing actions, with the resulting gridded vectors written into binary files "current.ww3" and "wind.ww3" at each output time step. Regions and time ranges for output of RTI values will be specified in the files *ww3_outp.inp* and/or *ww3_outf.inp*.

As usual, the current and wind data are allowed to vary in time and space. Spatially varying fields are read in via the **ww3_prep** program, using instructions in the *ww3_prep_*.inp* user-input files. Otherwise, the user can employ the simpler option of specifying them as homogeneous (but potentially time-varying) fields via the **ww3_shel** program, using instructions in the *ww3_shel.inp* user-input file. The **ww3_prep** approach of WW3 supports a number of different methods of user input. For example, the user can provide the wind velocity components as ascii files on a non-WW3 grid, and **ww3_prep** will interpolate in time and space to the WW3 computational grid(s).

For the immediate future, the WW3 code and test cases described in this report will be maintained on a branch of the NRL svn repository, whose master branch was last synchronized with the trunk of the NCEP svn repository at revision r1051 (NCEP revision c89b58e was modified to revision d7af8f1 on May 17, 2018). The latest update to the NRL svn repository (from the new GitHub platform) at time of writing was r1443.

3 ROGUE THREAT INDEX – THEORY AND IMPLEMENTATION

The theory and implementation of the rogue threat index and its components are described in this section. The RTI itself is designed as a scalar value computed by a separable function of four causal factors, which include nonlinear frequency modulation, adverse current gradients, wave direction effects, and wind effects. The function might be written most simply as

$$RTI = f(C_{BFI}, C_{curr}, C_{dir}, C_w) \tag{2}$$

in which each of the component causal factors is either a scalar or a logical (i.e., true/false). As noted, this analysis assumes that the effects of the four factors are separable, so that each one is first computed on its own from the physical datasets and then combined with the others through multiplication or a conditional statement (as described below). While we acknowledge that this assumption may produce some inaccuracy, we would argue that it is likely to be a reasonable approximation, particularly in the case of nonlinear modulation and adverse current gradients (see Sections 3.1.1 and 3.1.2). We view this software package as a "first edition", anticipating that future research and development will steadily improve its accuracy and effectiveness.

3.1 Theory: Rogue Wave Causal Factors

The subsections below detail the theoretical, numerical, and experimental bases supporting each of four environmental phenomena that we have selected as primary causal factors contributing to or limiting rogue wave development. The relationships described here were further validated and quantified by (primarily numerical) investigations that will be covered in Section 3.2.

3.1.1 Frequency modulation and the Benjamin Feir Index (BFI)

Rogue waves are generally more likely to occur under conditions characterized by wave frequency spectra with energy concentrated in a narrow bandwidth. In such an environment, resonant nonlinear interactions can force a *modulational instability*, or rapid energy exchange between individual spectral components (Kharif & Pelinovsky, 2003), leading to accelerated growth of waves at specific frequencies. This result has been illustrated in simulations with mathematical models that make use of dispersive partial differential equations (Manzetti, 2018) and demonstrated experimentally in wave flumes (e.g., Chabchoub et al., 2011)

The concentration of energy over a narrow spectral bandwidth can results increased steepness of the waves in that bandwidth, which is directly correlated with the level of nonlinear behavior of the system (Hjelmervik & Trulsen, 2009). The breaking of waves is closely related to their steepness, which is normally measured as $\epsilon = ak$, where a is wave amplitude and k is wave number. Progressive waves will break when their steepness exceeds approximately 0.45 (Toffoli et al., 2010), while waves in a spectrum have been shown to break with an average steepness around 0.2 (Chalikov and Babanin, 2012).

In recent decades, various research efforts have investigated modulational instability in wave spectra and attempted to quantify the related conditions. A widely accepted metric for assessing the risk of rogue wave appearance via modulational instabilities in random sea states is the Benjamin–Feir Index (BFI), a ratio of wave steepness to spectral frequency bandwidth. There are multiple (generally equivalent) methods for computing BFI. The name was first proposed by Janssen (2003), who derived a version of the index from the Zakharov equation (Zakharov 1968). A similar expression was developed earlier by Onorato et al. (2001). For this project, we have elected to use a more recent formulation of BFI from Rogers and van Vledder (2013):

$$BFI = \sqrt{2\pi} k_p \sqrt{E_T} Q_D \tag{3}$$

where k_p is the peak wavenumber of the spectrum, $E_T = \int E(f) df$ is the total wave energy integrated over all frequencies f, and the frequency narrowness parameter Q_D is computed according to Goda (1970) as:

$$Q_D = \frac{2 \int E^2(f) f df}{E_T^2} \tag{4}$$

The formulations given by equations (3) and (4) were utilized in numerical testing by Manolidis et al. (2019) to investigate the effects of current gradients on rogue wave development, as will be detailed in Section 3.1.2 below. BFI values greater than unity indicate a significantly higher risk for a rogue wave incident. Wave conditions such as these are also characterized by wave height probability distributions that deviate from the Gaussian norm, displaying an increased likelihood for the occurrence of extreme waves in general.

Babanin et al. (2011) suggest that for the steepness range $\epsilon \sim 0.11$-0.13, narrow-banded wave spectra are particularly responsive to the Benjamin-Feir instability, growing rapidly due to

nonlinear modulation but not yet steep enough to break. Waves in this steepness range are thus considered most likely to develop into rogue waves.

3.1.2 Adverse current gradients

Very strong currents, such as those occasionally found at river mouths, can cause the development of rogue waves in a manner consistent with linear theory. When an opposing current has a magnitude near the phase velocity of approaching waves, it produces an extreme Doppler shift in the waves, slowing their net speed and causing a wave group to "pile up" into a single abnormally large and steep crest. The current induces wave focusing at the blocking point. This phenomenon has been encountered in coastal waters near the mouth of the Columbia River in the northwestern U.S. (e.g., Johnston, 2014). It is already included in estimates of wave spectral propagation produced by WW3.

In contrast, nonlinear theory allows for energy to be transferred between currents and interacting spectral components. The modulational instability, described in the preceding section, can be enhanced when nonlinear waves propagate into an opposing current that increases in magnitude as the waves progress forward (Figure 1)[1]. Through these nonlinear processes, such adverse current gradients can either induce a new modulational instability or amplify an existing one. When a wave group encounters such a current (assuming it is not strong enough to cause linear blocking), energy is transferred from the flow field to the overlying waves, which both steepen and grow larger. The transfer process favors the more energetic waves near the peak frequency, which effectively narrows the frequency bandwidth of the overall spectrum (Onorato et al., 2011; Ruban 2012). The currents also increase wave steepness via a Doppler shift effect. In combination, these changes produce a wave packet with increased modulational instability, leading to a greater BFI.

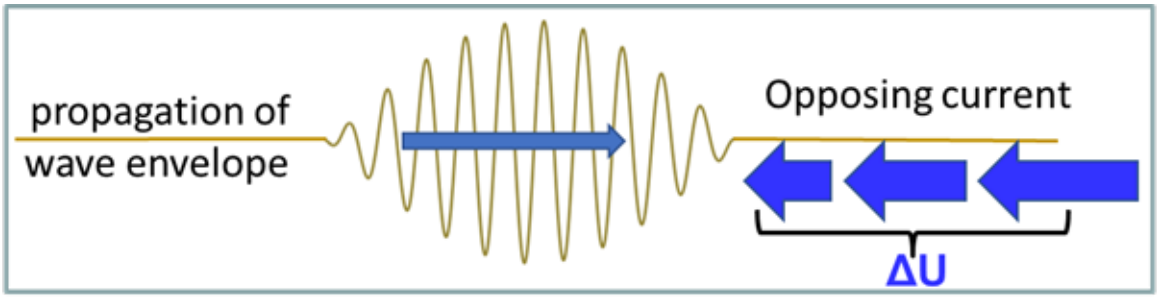

Figure 1. Illustration of wave group propagating into an adverse current gradient. As the wave group propagates from left to right, the opposing current grows stronger.

There appears to be some anecdotal evidence of this effect in ocean boundary currents. For example, in the region of the Agulhas current off the southeast coast of Africa, huge rogue waves have been reported on multiple occasions. Several large ships have been severely damaged or sunk by rogue waves in that area, and, in some cases, dozens of people lost their lives (Lavrenov 1998).

[1] Nonlinear wave growth may also result when waves propagate in the same direction as ocean currents that are *vertically* sheared (i.e., the current magnitude decreases with depth). Some evidence for this is provided by Choi (2009). This effect will not be addressed in the present formulation of the RTI; however, it may be incorporated in a future version.

As part of this project, Manolidis et al. (2019) used a series of numerical simulations with the non-hydrostatic, finite volume model NHWAVE (Ma et al., 2012) to quantify the increase in spectral nonlinearity that results from adverse current gradients of different strengths. When the nonlinearity is represented by the BFI, they determined that the effect of adverse current gradients could be expressed as

$$BFI_1 = BFI_0 exp\left(\alpha \Delta U_{01} / c_g\right) \quad (5)$$

where BFI_0 and BFI_1 are the BFI value at initial location ("0") and after propagating to a new location ("1"). BFI_0 is computed using equation (3), α is an empirical constant that was determined to be approximately 5.3, ΔU_{01} is the absolute increase in the adverse current magnitude between locations 0 and 1, and c_g is the group velocity for the wave packet. Note that the current gradient, ΔU_{01}, is computed only from the components of the current that are directly opposing the peak wave propagation. Components of the current that are perpendicular to the wave propagation direction are not used here.

More recent work by co-author Michail Manolidis (not yet published) provides evidence that a similar increase in BFI will result from a *decreasing* current that is traveling *in the same direction* as the waves. In such a scenario, the waves are propagating on top of a current with speed U_0, which tapers off to a slower speed U_1 but continues to propagate in the same direction as the waves. Such conditions might be found near the point where a boundary current separates from a continent or where an eddy begins to separate from a larger flow. The value of ΔU_{01} is again negative in this case, and simulations by Manolidis indicate that the effect on BFI is essentially the same as described by equation (5) above.

3.1.3 Wave directional distribution

The superposition of waves, a cumulative increase in total crest height that occurs when multiple waves simultaneously pass the same point, is primarily a linear phenomenon. It can occur when longer, faster waves pass smaller, slower waves traveling in the same direction, or when two or more wave systems converge from different directions. Babanin et al. (2011) found that directional focusing of wave fronts could rapidly double deep-water wave height and steepness, frequently resulting in dangerous breaking waves. A sea state in which two or more wave systems of similar peak frequency converge can thus be quite hazardous, even without the presence of modulational instabilities contributing to further growth of rogue waves.

The linear summation of converging wave heights is included in numerical models such as WW3; therefore, it will not be included in the rogue threat index computation described herein. However, this effect can be dampened or augmented – in a manner not currently represented in operational wave models -- by nonlinear modulation in directionally narrow wave distributions or crossing seas (Gramstad et al., 2018; Onorato et al., 2009; Cavaleri et al., 2012). It was qualitatively demonstrated by Onorato et al. (2009) and Waseda et al. (2009) that frequency modulation in typical JONSWAP-type unimodal spectra is inversely correlated with their directional spread (i.e., steep waves with directionally narrower spectra exhibit increased frequency modulation). It has also been demonstrated by several investigations that crossing sea states (in which two wave fronts approach from different directions) can affect the nonlinearity of the resulting waves (e.g., Toffoli et al., 2011).

As a means of quantifying the effect of directional spread on modulation, Babanin et al (2010) proposed the directional modulation index:

$$M_{Id} = A \cdot \epsilon \tag{6}$$

where A is a representation of directional narrowness ranging between 0.8 – 1.8 (Babanin & Soloviev, 1998). As noted earlier, the term $\epsilon \sim ak$ represents the mean product of the wave field's amplitudes and wave numbers (i.e., mean wave steepness). Based on laboratory experiments, Babanin et al (2011) suggested that modulational instability would occur in wave conditions for which $M_{Id} > 0.18$.

Mori et al. (2011) used Monte Carlo simulation results to develop a modified directional BFI, expressed as

$$BFI_{2d} = {BFI}/{\sqrt{1 + 7.1R}} \tag{7}$$

where R is a ratio of directional spread to frequency bandwidth. While we will be making use of this simplified approximation here (see Section 3.2.3 below), we acknowledge that the role of wave direction in rogue formation can be considerably more complicated. For example, Ruban (2012) suggests that spectral shape should also be considered in estimating directional effects, while Babanin (2013) notes that the short-crested, three-dimensional shapes of individual wave crests can also be important.

For bimodal distributions with two distinct directional peaks (i.e., crossing seas), the picture is perhaps even less clear. There is evidence that specific ranges of crossing angle will enhance nonlinear modulation of the wave spectrum more than others. However, there is not unanimous agreement about which angle ranges are associated with the greatest amplification and growth rate. Toffoli et al. (2011) and Cavaleri et al. (2012) use lab experiments and coupled Nonlinear Schrödinger Equations (NLSE) to demonstrate that spectral nonlinearity and kurtosis are most elevated in crossing sea states with a bimodal angle between 40° – 60°. They caution, however, that crossing seas in the ocean can be much more complicated than the simulations they conducted.

More recent work by Gramstad et al. (2018) suggests that linear and nonlinear effects of crossing seas are, in fact, complementary. Their results generally indicate that linear superposition effects of crossing seas are greatest for angles near 90°, but nonlinear growth effects (measured by kurtosis and peak wave crests) are greatest for smaller (10° – 30°) and larger (150° – 180°) angles and weakest near 90°. This conclusion is supported both by theoretical investigations with two crossing Stokes waves and by HOS simulations with directionally spread JONSWAP spectra. For highly nonlinear, directionally narrow-banded crossing seas (i.e., JONSWAP $\gamma = 6$, directional cosine power $N = 100$), the modeled results display a local peak at roughly 45°, in support of the earlier findings by Toffoli and Cavaleri.

Gramstad et al. (2018) also investigate variations in kurtosis and maximum wave height that result when the two peak amplitudes or periods of a bimodal spectrum are not equal. For nonlinear, narrow-banded spectra, their simulations suggest that these rogue wave markers are largest when the two peak amplitudes and/or periods are equal, weakening consistently as differences between the two peaks increase.

Onorato et al. (2010) investigate both the growth rate and the amplification factor produced by crossing seas involving two wave systems of equal amplitude and peak frequency. Although they find large amplification factors for crossing angles near 35°, they conclude that rogue waves are unlikely under these conditions because the associated growth rates are small. Considering both effects together with modeled kurtosis results, the authors suggest that the highest probability of rogue waves occurs for bimodal angles between 10° – 30°, where amplification, growth rate, and kurtosis are all larger than average. As in the above-cited studies, the authors acknowledge that the conditions of their simulations are simplified compared to those of the 3D ocean environment.

3.1.4 Wind effects

In the early stages of wave growth, wind forcing at the water surface tends to add energy to the wave spectrum, primarily at higher frequencies. However, at later developmental stages, when steeper, highly nonlinear wave crests have evolved and are approaching rogue status, even gentler winds can act to dampen the modulational instability and slow or limit growth of the saturated wave (Trulsen & Dysthe, 1992; Babanin et al., 2010). This damping effect appears to grow stronger as wind speed (in the same direction as waves) increases. Galchenko et al. (2012) determined that for 1D waves with steepness $\epsilon = ak = 0.17 - 0.23$ (where a is amplitude and k is wave number of the primary carrier wave), the lower sideband of a carrier wave was most suppressed when the ratio of wind speed over wave celerity, U/c, was in the range 4 – 8. For extreme winds approaching hurricane speeds (i.e., U_{10}>33m/s), Babanin (2011) suggests that conditions in the atmospheric boundary layer will change such that nonlinear interactions no longer drive the evolution of the waves, inferring that this will reduce likely maximum wave heights and rogue wave occurrence in more powerful storms. This conclusion is supported by earlier theoretical analysis from Trulsen and Dysthe (1992) and laboratory work by Bliven et al. (1986).

3.2 WW3 Code: Numerical Implementation of Rogue Threat Index

The methods of user-input to WW3 have already been explained in Section 2. In this section, we describe the numerical methods used to implement the four rogue threat index components corresponding to each of the causal factors detailed immediately above. In the initial release version of this RTI software, the index is computed as a function of four separable components, each of which individually represents the relative contribution of a one of the four environmental causal factors discussed in Section 3.1. In contrast to the theoretical method for estimating space-time extremes implemented in WW3 and described by Barbariol et al. (2017), this threat index computation is primarily based on empirical results that quantify existing theoretical relationships for each causal factor. The utility is intended to evolve and be adaptable, and it is expected that future versions of the RTI will incorporate additional physics, validation data, and contributions of additional causal factors (e.g., bathymetric effects in shallower coastal regions).

3.2.1 Component 1: BFI (C_{BFI})

The first component of the formulation consists simply of a computation of the Benjamin-Feir Index (BFI). As noted in Section 3.1.1, a range of roughly equivalent expressions has been developed for this index. For this software utility, we will adopt the same formulation specified in equation (3) earlier from Manolidis et al. (2019); i.e.,

$$C_{BFI} = \sqrt{2\pi} k_p \sqrt{E_T} Q_D \tag{8}$$

In the numerical implementation of (8), the frequency narrowness parameter Q_D is computed at each grid location by integrating the product of the frequency and the spectral density provided by WW3, then dividing the result by the square of the total spectral energy E_T. Peak wavenumber k_p is determined from the dispersion relation as the wavenumber corresponding to the peak frequency, f_p.

3.2.2 Component 2: Current gradient multiplier (C_{curr})

The formulation used for the current gradient component of the rogue threat index is a numerical adaptation of the exponential term on the right-hand side of equation (5). The only part of this term that must be computed is the current gradient, ΔU_{0l} (Group velocity, c_g. is obtained from the WW3 restart file). As noted in section 3.1.2, the direction of the flow field relative to the waves is not important, only that the current gradient is negative. The numerical computation of the current gradient for a wave spectrum at grid location (i, j) is performed as follows. The magnitude U and direction θ_c of the current vector $\vec{U}$ may be used to divide it into E-W ($\hat{\imath}$) and N-S ($\hat{\jmath}$) directed components

$$\vec{U} = \hat{\imath}Ucos\left(\theta_{c,i,j}\right) + \hat{\jmath}Usin(\theta_{c,i,j})$$

where $\theta_{c,i,j}$ is the direction in which the current is traveling at location (i, j), in degrees counterclockwise relative to the model x-axis. We begin by computing three-point-averaged x- and y-components of the current vector $\vec{U}$ on opposite sides of the spectrum location (see Figure 2).

$$\overline{U}_{x,i-1} = \frac{1}{3}\sum_{J=j-1}^{j+1} U_{i-1,J}\sin\left(\theta_{c,i-1,J}\right)$$

$$\overline{U}_{x,i+1} = \frac{1}{3}\sum_{J=j-1}^{j+1} U_{i+1,J}\sin\left(\theta_{c,i+1,J}\right)$$

$$\overline{U}_{y,j-1} = \frac{1}{3}\sum_{I=i-1}^{i+1} U_{I,j-1}\cos\left(\theta_{c,I,j-1}\right)$$

$$\overline{U}_{y,j+1} = \frac{1}{3}\sum_{I=i-1}^{i+1} U_{I,j+1}\cos\left(\theta_{c,I,j+1}\right)$$

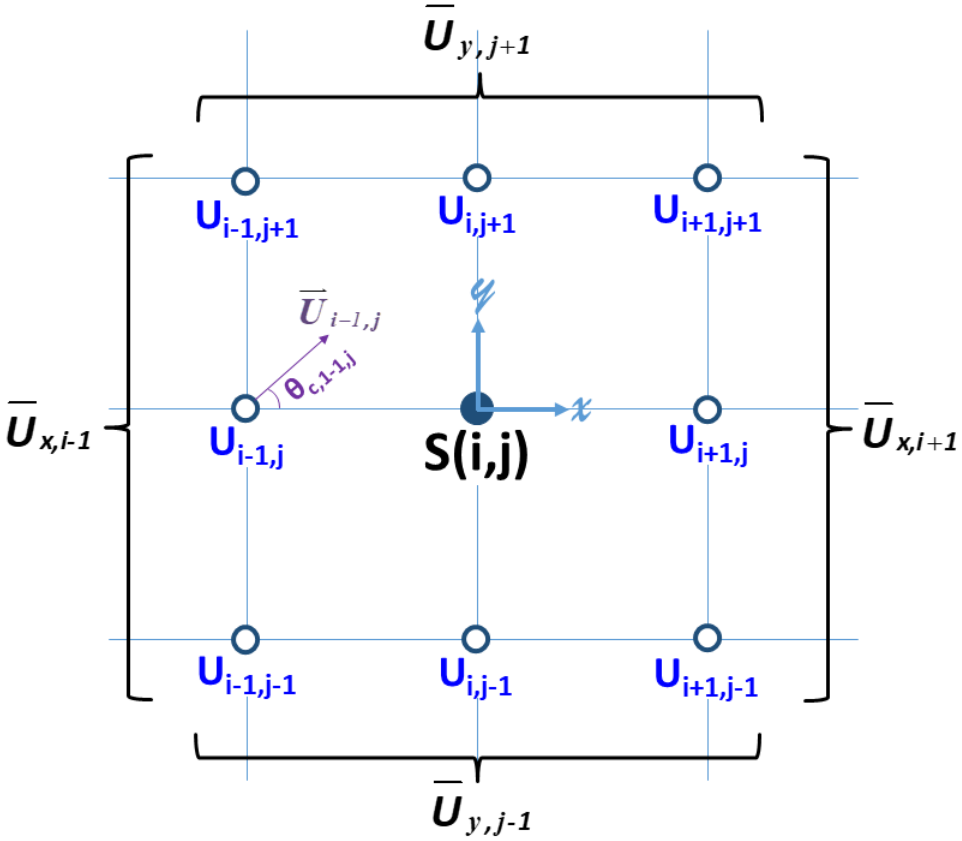

Figure 2. Grid reference for computation of ΔU in current gradient component of rogue threat index.

The current gradients in the *x*- and *y*-directions are then computed from the mean current components on each side, followed by the resultant current gradient magnitude and direction.

$$\Delta U_x = (\overline{U}_{x,i+1} - \overline{U}_{x,i-1})/(2\Delta x) \tag{9}$$

$$\Delta U_y = (\overline{U}_{y,j+1} - \overline{U}_{y,j-1})/(2\Delta y) \tag{10}$$

$$\Delta U = \sqrt{(\Delta U_x)^2 + \left(\Delta U_y\right)^2} \tag{11}$$

$$\theta_c = \tan^{-1}\left({\Delta U_x}/{\Delta U_y}\right) \tag{12}$$

where Δx and Δy are the grid spacing in x and y directions. The resultant overall current gradient in the direction of wave travel, ΔU_{01}, is then obtained by computing the projection of the current gradient vector ΔU onto the mean wave direction θ_w:

$$\Delta U_{01}(i,j) = \Delta U \cos(\theta_{cw}) \tag{13}$$

Here, $\theta_{cw} = \theta_w - \theta_c$ is the angle between the mean current gradient direction, θ_c, and the mean Cartesian wave direction, θ_w (see Figure 3)[2]. The distance from location "0" to location "1" is

[2] The Cartesian wave direction mean direction *toward* which the waves are propagating, following the Cartesian convention. This contrasts with the common nautical convention in which spectral angles describe the direction waves are coming *from*.

arbitrary, in that it will only affect the scale of the RTI when combined with other RTI components. In the present WW3 implementation, we multiply the result of (13) by $\Delta X_{01} = 1000m$ to convert it from units of $[m/s]/m$ to units of m/s.

As noted above, only a *negative* current gradient will increase the modulation of a given wave state. Consequently, the computed value of ΔU_{01} from equation (13) is utilized in the following conditional expression to determine C_{curr}, the current gradient component of the rogue threat index:

$$C_{curr} = exp\left(5.3 \cdot |\Delta U_{01}|/c_g\right) \quad if \quad \Delta U_{01} < 0 \qquad (14)$$

$$C_{curr} = 1 \qquad otherwise$$

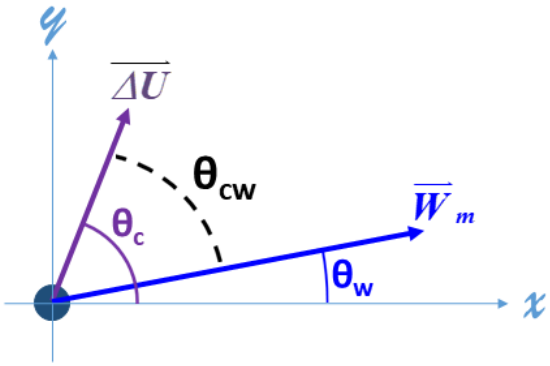

Figure 3. Determination of relative current gradient angle, θ_{cw}, from mean current gradient direction, θ_c, and mean wave direction, θ_w. The latter two angles are both measured counterclockwise from the modeled x-axis.

3.2.3 Component 3: Directional spread and crossing seas (C_{dir})

As noted in Section 3.1.3, increasing directional spread consistently reduces the likelihood of rogue wave occurrence, while different values of directional bimodality angle in crossing seas appear to cause irregular variations in spectral kurtosis and rogue wave occurrence. Accordingly, in the computation of this effect, we will divide the wave direction causal factor C_{dir} into separate components for directional spreading ($C_{dir,s}$) and bimodality ($C_{dir,b}$).

Directional Spread

Although the results provided in Section 3.1.3 pertaining to the effects of directional spread are generally consistent among multiple studies, we nevertheless conducted a brief series of phase-resolved, 3D HOS simulations to obtain basic confirmation of these results. The higher-order spectral model HOS-ocean (Ducrozet et al., 2016) was initialized with frequency-directional spectra defined by combining a JONSWAP frequency distribution with a cosine-power directional spread. Two configurations were tested with each based on the same JONSWAP spectrum, but with one using a cosine-squared directional distribution while the other used an essentially infinite-power cosine distribution (i.e., the code was configured to assign all spectral energy to frequencies in a single directional bin). Four simulations were run simultaneously in a 2700m by 700m domain for each configuration, with wave phases differently randomized in each case.

Along the center line of the domain, wave crest heights η_{crest} were measured and significant wave height H_s was computed at each time step. The total wave count for each test configuration exceeded 800,000. Values of η_{crest} / H_s were compiled across each set of four simultaneous tests to produce an exceedance probability distribution for the directionally broad and narrow initializing spectra (Figure 4). As illustrated in the figure, the directionally narrow distribution (N = Inf) is significantly more skewed toward larger crest heights, producing over 80 crests that met the rogue wave criterion (i.e., $\eta_{crest} \geq 1.25 \cdot H_s$). In contrast, the broad distribution (N = 2) produced only a few such anomalously large waves. Our results are very similar to earlier published results from Onorato et al. (2009; see their Fig. 4).

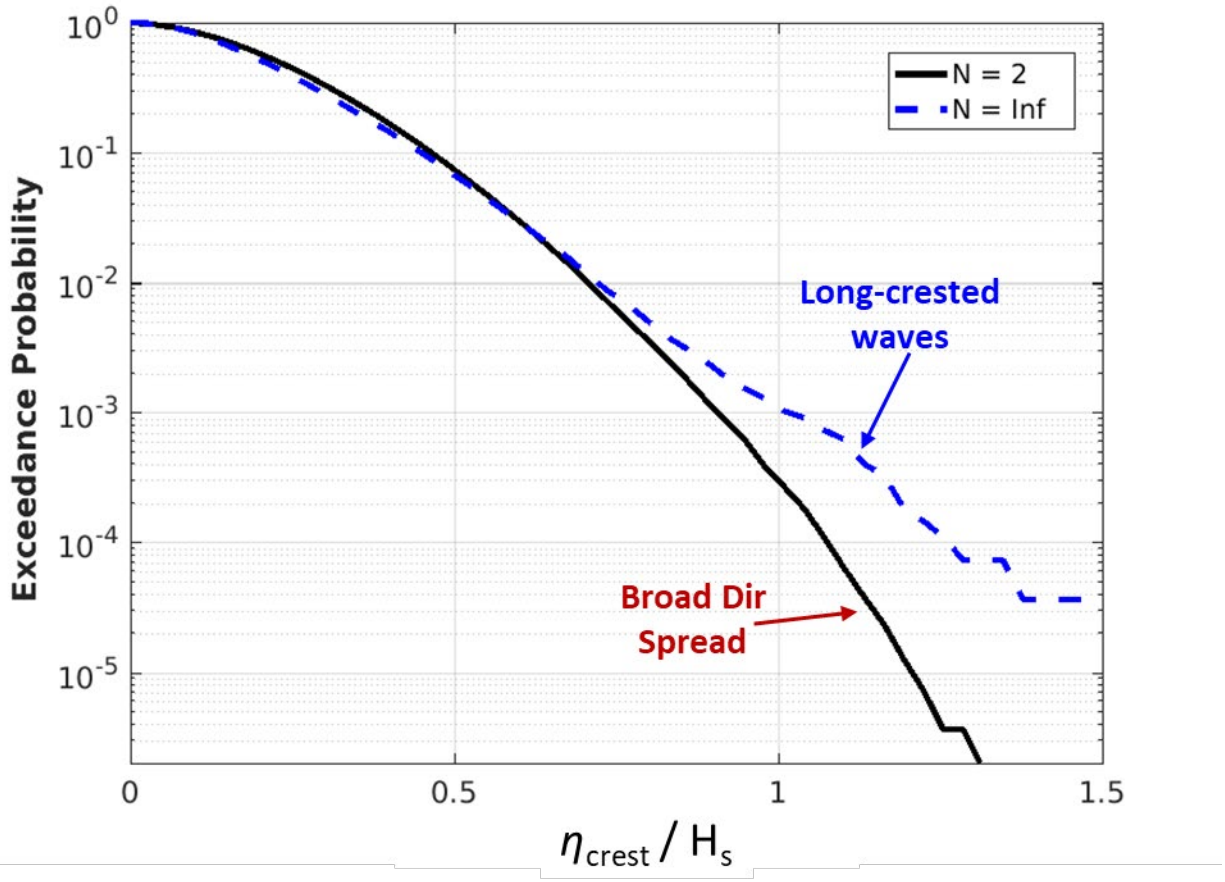

Figure 4. Simulation results for exceedance fraction of all waves plotted versus the ratio of crest height to significant wave height. From four simultaneous simulations with random wave phases, utilizing JONSWAP frequency spectrum with $cos^N(\theta-\theta_o)$ spreading function, with either N=2 (black line) or N=Infinity (blue dashed line).

Following this qualitative confirmation of the conclusion of multiple published studies, we elected to use existing, previously developed representations of the nonlinear effects of directional spread in our computation of $C_{dir,s}$. These effects were thus incorporated into the rogue threat index computation via the expression of Mori et al. (2011), as given in equation (7) above. The directional spread component of C_{dir} consists of the inverse root portion of that equation:

$$C_{dir,s} = {}^{1}/_{\sqrt{1+7.1R}} \tag{15}$$

where R, the ratio of angular to frequency bandwidth in the spectrum, is computed as

$$R = \frac{1}{2}\frac{\delta_\theta^2}{\delta_\omega^2} \tag{16}$$

Angular bandwidth, δ_θ^2, is computed from the 1D directional spectrum (i.e., after integrating the WW3 spectrum over frequency), while frequency bandwidth, δ_ω^2, is computed from the 1D frequency spectrum (i.e., after integrating the WW3 spectrum over direction).

Crossing Seas (Bimodality)

Directional bimodality effects from crossing seas are incorporated into the rogue threat index using an empirical representation based on our own model simulations. The studies cited in Section 3.1.3 above generally agree that nonlinear effects of crossing seas tend to diminish as the crossing angle increases from 0°. However, several also suggest that there is at least a local peak in kurtosis and/or rogue likelihood for a bimodal angle of approximately 40°-60° (with Gramstad et al. (2018) noting that a peak occurs at 45° only for spectra that are narrow-banded in both frequency and direction).

To validate and further quantify these effects, we conducted a series of additional simulations with HOS-ocean. First, a new series of 3D simulations was conducted in which each test was initialized with waves corresponding to a directionally bimodal spectrum with two equal amplitude peaks that were narrow in both frequency and direction (e.g., Figure 5). Bimodal angles between the two peak directions ranged from 0° to 170°. The same domain size (i.e., 2700m by 700m) was used here as in the earlier directional spreading tests. For each test, four separate simulations were again run simultaneously, with each using the same bimodal angle and initialization settings but different wave phase randomization. For each set of four simulations, we calculated wave height distribution, maximum kurtosis, maximum rogue wave height (relative to H_s), and the number of rogue waves occurring in the entire set. Results are summarized below and in Figure 6 - Figure 9.

There were more large waves in the distributions for test sets involving smaller bimodal angles (i.e., 0° and 30° angles in Figure 6), while most large angles (e.g., 60°, 90°, 170°) exhibited a smaller proportion of rogues (if any). Anomalously low results was also obtained for the bimodal angles of 46° and 48° (magenta and yellow lines in Figure 6). These results were clearly reflected in the tally of total rogue waves at each angle (Figure 7), for which 0° and 30° again lead the pack. However, this figure also includes an unusual "bump" in between bimodal angles 34° – 48°, for which the number of rogues increases to a local peak around 45°.

This local peak is also seen in the plot of maximum rogue crest height relative to H_s (Figure 8) and to a lesser degree in the plot of maximum kurtosis (Figure 9). The latter figure in particular illustrates a result that is at least qualitatively similar to that seen in Gramstad et al (2018; Fig 7a, green line).

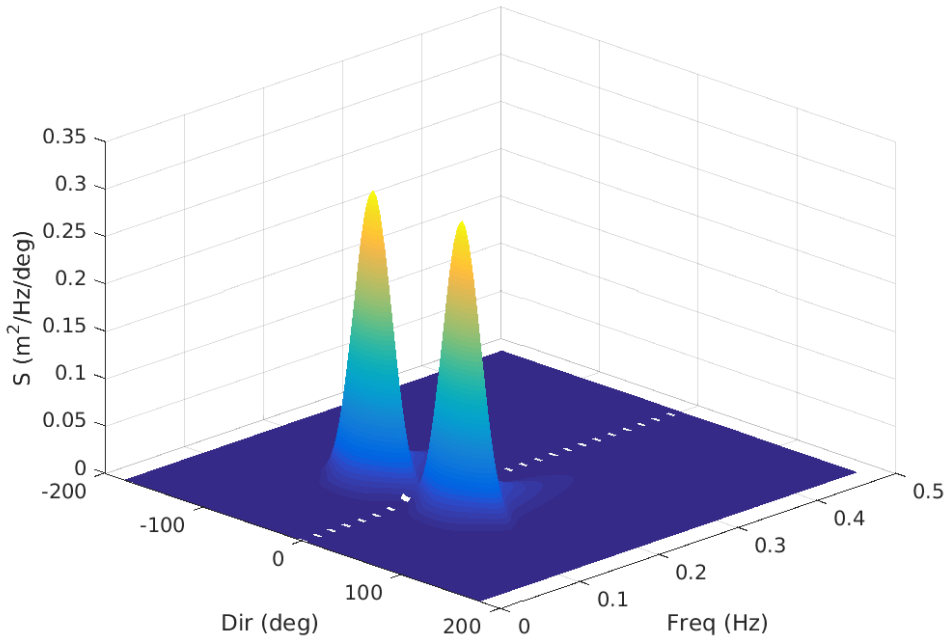

Figure 5. Example of directionally bimodal spectrum with two narrow peaks of equal amplitude separated by 90°. Waves generated by HOS-ocean that were based on this spectrum and others were used to investigate the effects of crossing seas angles on rogue wave development.

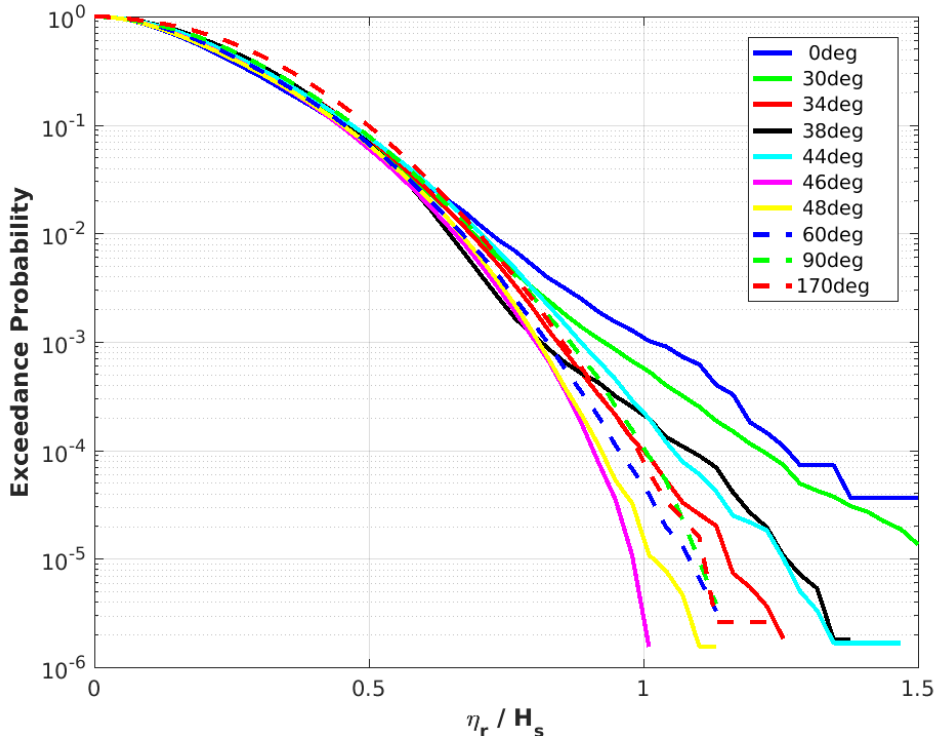

Figure 6. Exceedance probability distributions of wave heights from HOS simulations for crossing seas with a range of different bimodal angles (0° – 170°).

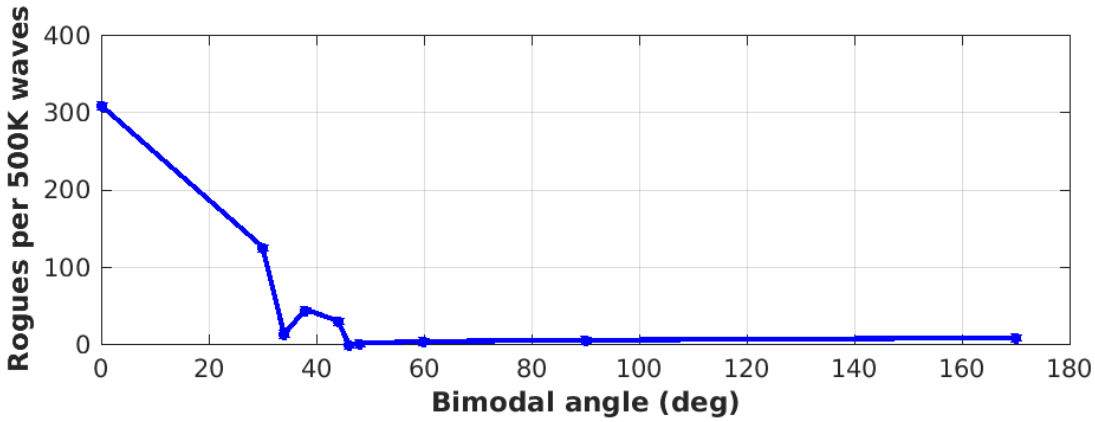

Figure 7. Number of rogues counted in HOS simulations (normalized as "per 500k waves in simulation", as different simulations had a different total number of counted waves), plotted versus bimodal angle of initializing spectrum.

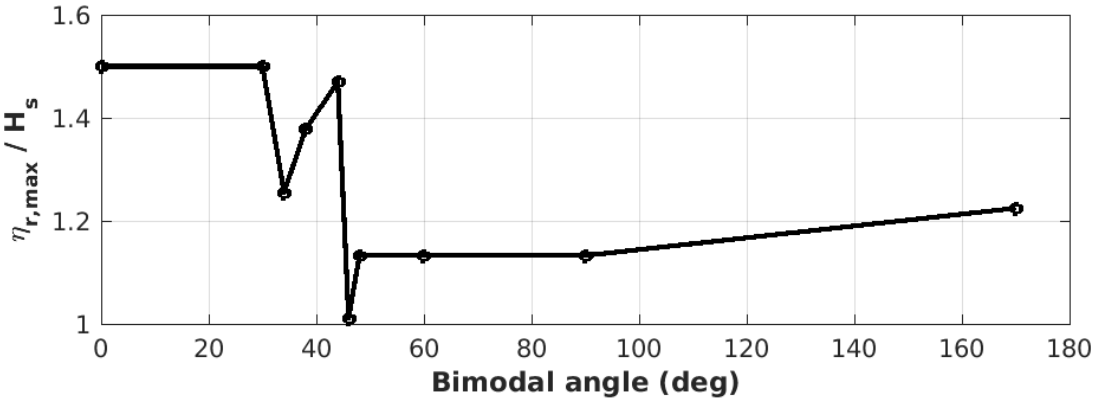

Figure 8. Maximum rogue wave surface elevation in HOS simulations relative to significant wave height (i.e., η_r / H_s), plotted versus bimodal angle of initializing spectrum.

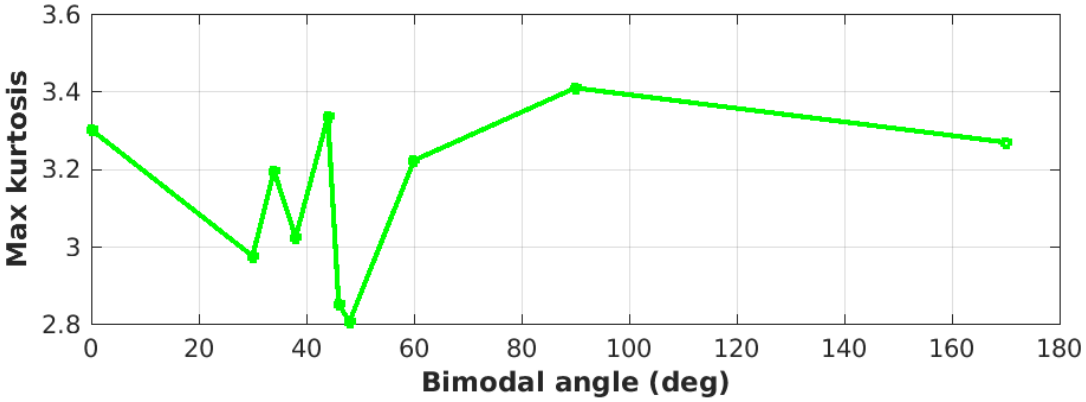

Figure 9. Maximum kurtosis in HOS simulations, plotted versus bimodal angle of initializing spectrum.

While the kurtosis results in Figure 9 above are somewhat inconclusive, Figure 6 – Figure 8 all consistently indicate a decrease in rogue wave frequency and maximum height as the crossing angle increases from 0° in bimodal spectra. Although we have found some evidence of a "bump" in likelihood in the angle range 35° – 50°, the number of occurrences associated with the peak of this bump is generally small compared to those measured for smaller angles. In summary, we conclude from our results that rogue wave likelihood will be ***reduced*** for bimodal spectra, with greater bimodal crossing angles producing greater reduction in rogue wave occurrence. These results are most consistent with those of Onorato et al. (2010; especially their Fig. 6).

As noted in Section 3.1.3, Gramstad et al. (2018) found that differences between the peak amplitude and/or period of two crossing systems would result in lower kurtosis and smaller rogue waves, in comparison to the case when both bimodal peaks were roughly equal in size and frequency. We conducted several additional simulations to validate these results with HOS-ocean, limiting the tests to bimodal angles $\theta_b = 30°$ and 44°. In the peak amplitude tests, the ratio of significant wave height associated with each system, $H_{s,1} / H_{s,2}$, was configured to be either 1, 2, or 3. In the peak period tests, the ratio of peak periods of the two systems, $T_{p,1} / T_{p,2}$, was set to one of the same three values. The paired values were adjusted so that the overall significant wave height and peak period of the combined system remained approximately constant (i.e., $H_{s,12} \approx 0.42$m; $T_{p,12} \approx 4.5$s) throughout all the tests. Results of these tests are shown in Figure 10. Our simulations generally agree with those of Gramstad et al. (2018); i.e., maximum rogue height and kurtosis do generally decline (with a single exception[3]) as the difference between the crossing systems increases. Also included in the figure are panels showing the total number of rogue waves for each simulation (bottom panels), which consistently declines as well.

[3] Although we repeated the tests for $H_{s1} / H_{s2} = 1$ and 2, the rerun results in each case were very consistent with the original values. While maximum rogue height and number of rogues were larger when the peaks were equal, maximum kurtosis values were always anomalously large for the $H_{s1} / H_{s2} = 2$ case. Note that this value was by far the largest kurtosis result we obtained from any of our tests. We do not presently have an explanation for this result.

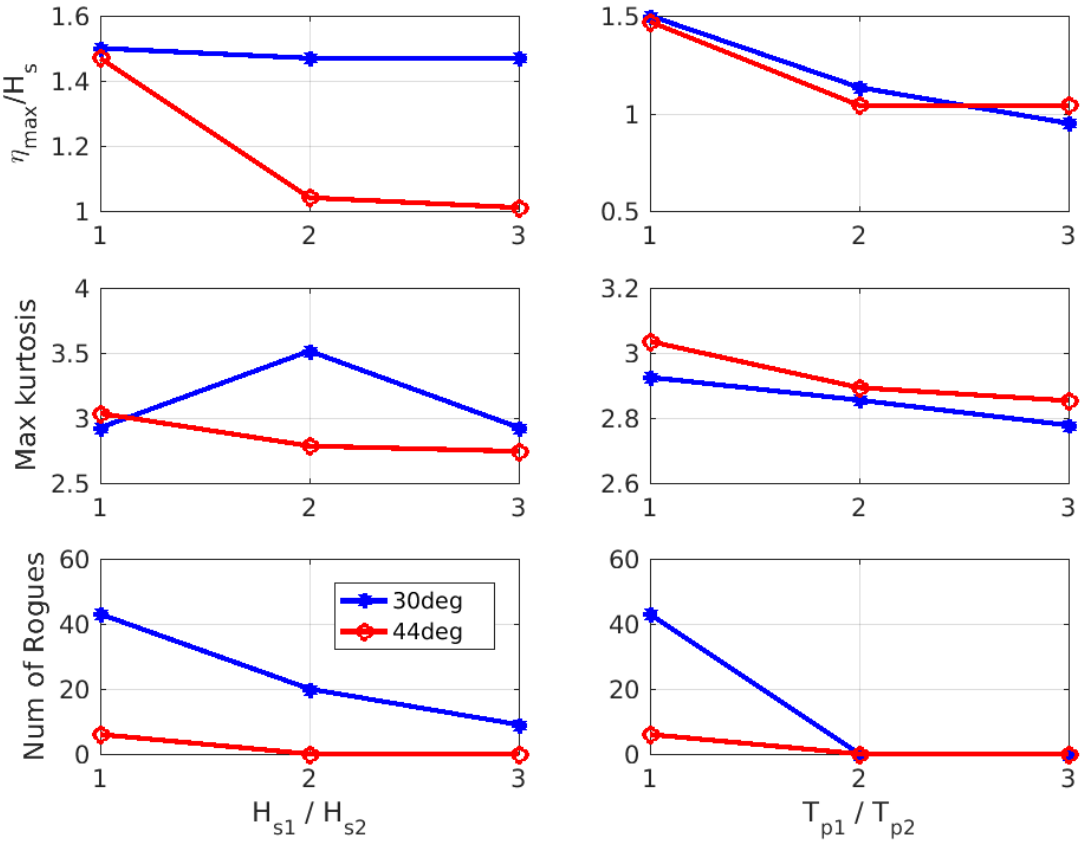

Figure 10. Variations in maximum rogue crest height (top panels), maximum kurtosis (middle panels), and number of rogues (bottom panels) for HOS simulations with bimodal spectra in which we varied the ratio of either significant wave heights (left column) or peak periods (right column) of the two crossing wave systems. Results are shown for bimodal angles of 30° (blue asterisks) and 44° (red circles).

Thus, while crossing seas can contribute significantly to large waves through *linear* superposition (which is already accounted for in WW3), our findings indicate that bimodality in spectra consistently *reduces* the likelihood of rogue wave development due to *nonlinear* modulation (in agreement with earlier published results). The directional bimodality factor, $C_{dir,b}$, is therefore configured to reduce the RTI in all cases when spectra are bimodal, with a simplified formulation that qualitatively follows our results.

The value of $C_{dir,b}$ in the rogue threat utility is set equal to one except in cases where WW3 spectra are "operationally bimodal" in direction. This is determined by first integrating the 2D WW3 spectrum over frequency to obtain a directional distribution, then computing Sarle's bimodality coefficient (Ellison 1987):

$$\beta = \frac{\gamma^2+1}{\kappa} \tag{17}$$

Here, γ is the skewness and κ is the kurtosis of the directional distribution, and the value of β ranges from 0 – 1. Only for a value of β above 0.75 will the distribution be considered operationally bimodal. If so, $C_{dir,b}$ is then computed as follows:

$$C_{dir,b} = \left(1.0 - 0.5 \cdot \frac{\theta_b}{50}\right) \; for\; \theta_b < 50°$$

$$C_{dir,b} = 0.5 \qquad for\ \theta_b \geq 50° \tag{18}$$

As these spectral conditions appear to be relatively uncommon, it is likely that the bimodality component of C_{dir} will only rarely play a role in reducing the RTI. The combined effects of directional spread and bimodality are incorporated into the rogue threat index as separate components of a product that both act to reduce the RTI:

$$C_{dir} = C_{dir,s} \cdot C_{dir,b} \tag{19}$$

3.2.4 Component 4: Wind limitation effect (C_w)

As noted in Section 3.1.4, growth-limiting effects of wind tend to occur primarily for specific ranges of strong winds that are blowing in the same direction as the wave crests are traveling. We conducted a series of numerical simulations with the OpenFOAM model (Chen et al., 2014) to verify and quantify this effect. In these simulations random ocean waves traveled in a numerical wave tank, whose amplitudes were such that the frequency spectra were characterized by high narrowness values. The phase relation between the central frequency and the two sidebands was adjusted to favor the rapid development of the modulational instability. This development, with consequent rogue waves, was tracked by monitoring kurtosis values. Results from the simulations are summarized in Figure 11.

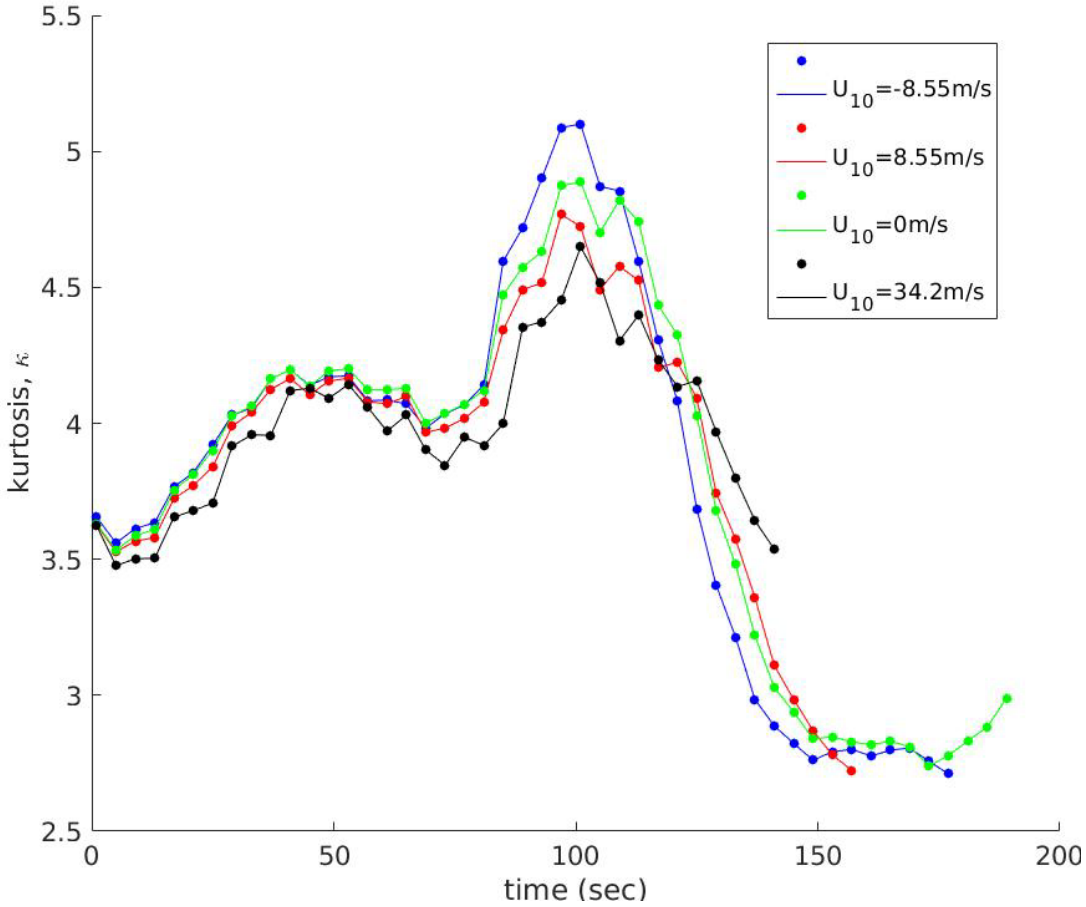

Figure 11. Kurtosis values in highly nonlinear waves propagating with or without wind, plotted against propagation time for four different configurations: wind directly opposes wave motion (blue); equilibrium wind in same direction as waves (red); waves-only simulation without wind (green); and hurricane-force wind in same direction as waves (black). Results are from 2D simulations with OpenFOAM. Wave group velocity is c_g = 8.55m/s.

In each simulation rogue waves appeared after approximately 100 seconds, as evidenced by elevated kurtosis values, but the severity of their development varied with wind speed and direction. Peak kurtosis values and rogue wave events occurred in the window 80sec < t < 120sec. In that time range, average kurtosis consistently declined as wind speed increased: the case of no wind resulted in $\boldsymbol{\kappa = 4.58}$; the case of equilibrium wind produced $\boldsymbol{\kappa = 4.47}$, and the case of hurricane-level wind (34.2m/s) reduced the value to $\boldsymbol{\kappa = 4.27}$. Interestingly, opposing wind (-8.55m/s) *increased* the severity of rogue wave development with mean kurtosis value rising to $\boldsymbol{\kappa = 4.70}$. These results agree well with published findings (Galchenko et al., 2012). Additionally, however, the simulations that we carried out were the first to replicate (a) random ocean conditions and (b) wind as a separate medium in two-phase flow.

As just noted, our results indicate that opposing winds appear to increase wave kurtosis for highly nonlinear waves, as illustrated by the blue line in Figure 11. While rarely mentioned in rogue wave literature, this result is in accord with commonly accepted surfer lore, which holds that the best surfing days are days when offshore-directed winds oppose and delay the breaking of shoaling waves, allowing them to grow taller. There appears to be no reason why this effect should not also apply to rogue waves. Although we have not fully addressed this question in the present analysis (or in the rogue threat utility), the effect of opposing winds is among the additional causal factors that we hope to quantify (and add to the RTI computation) in future research efforts.

For the time being, we will limit the quantification of wind effects only to cases of strong winds blowing in the same direction as the waves. With respect to the RTI computation, this effect will be implemented at each grid location and time step in WW3 by (a) determining mean wave direction from the local spectrum, (b) determining mean wind direction and magnitude from the gridded wind data (user must provide corrected formatted wind data for duration of the simulation). The magnitude of the component of wind (U_{10}) that is oriented in the same direction as the peak waves is computed as follows:

$$U_{10,w} = U_{10}\cos(D_m - W_m) \tag{20}$$

where D_m is the mean wave direction and W_m is mean wind direction. Here, the representation will be based on the results from the theoretical and modeling analyses described in Section 3.1.4. Strong winds will dampen rogue wave growth for specific ratios of wind speed, $U_{10,w}$, to mean wave speed, c (Galchenko et al., 2012), and when wind speeds reach hurricane levels (Babanin, 2011). This effect is incorporated into the coefficient C_w as a simple conditional:

C_w = FALSE ➔ under most wind and current conditions (21)

C_w = TRUE ➔ when $4 < {}^{U_{10,w}}/_{c} < 8$ or $U_{10,w} > 33\ m/s$

3.2.5 RTI computation from components

Because of the conditional form of C_w, the RTI computation itself is represented as a conditional expression, in which the type of computation is dictated by the presence or lack of extreme winds:

$RTI = C_{BFI} \cdot C_{curr} \cdot C_{dir}$ ➔ if C_w = FALSE (22)

$RTI = C_{BFI}$ ➔ if C_w = TRUE

In other words, when limiting winds are active in the prescribed ranges, only the BFI component C_{BFI} is used to compute the RTI. In the absence of such limiters, the complete RTI is computed, including effects of nonlinear modulation, adverse currents, and wave direction.

The value of the RTI is not presently normalized. Its magnitude can range from zero to roughly 5, depending on the exact combination of conditions, with larger values indicating a greater potential threat of rogue wave development. This range will be more precisely calibrated as part of the upcoming VTR process (see Section 5.1), in which the index value will be computed for a wide variety of conditions including both rogue events and calmer conditions.

The Fortran file containing these post-processing computations is named *ww3_rti.ftn*. Sample results from this function are presented in Section 4.3.

4 OUTPUT AND INITIAL TESTS OF ROGUE THREAT UTILITY

As presently designed, the utility is a post-processing program separate from the main WW3 code (Figure 12). It reads in files created by WW3, including spectral restart data, gridded ocean currents and gridded wind fields, then uses these data to compute the RTI for user-specified times and regions. WW3 can obtain current and wind data from a coupled system such as ESPC, or they may be provided as input files by the user. Output can include maps of rogue threat at global, regional, and local scales, combined maps of significant wave height and rogue threat, time series of evolving RTI values a specific locations, and maps of individual causal factor values (for identifying primary contributors to specific rogue threats).

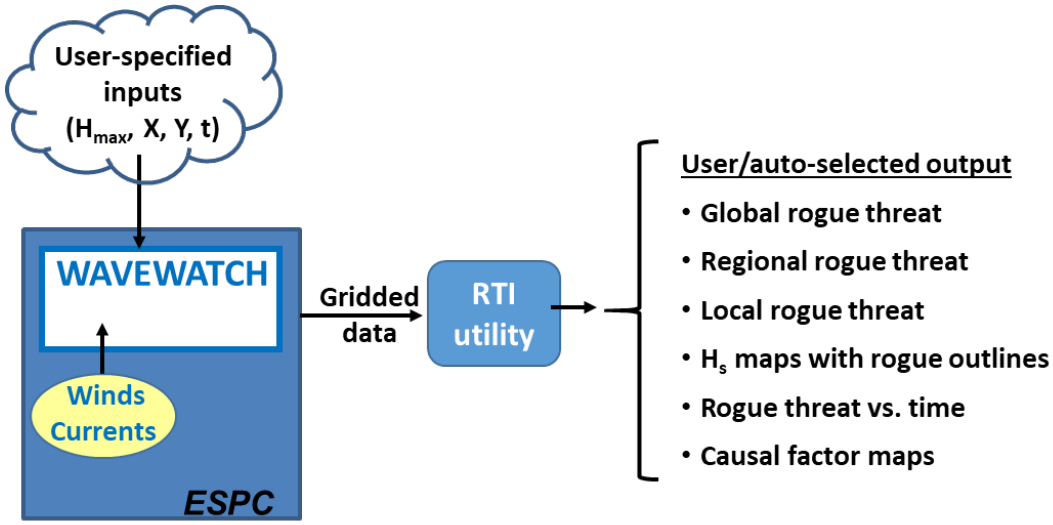

Figure 12. Flow chart of RTI utility within WW3 system.

As noted in the Introduction, stochastic wave spectra represent phase-averaged conditions and cannot be used to predict specific rogue events at specific times. As a consequence, testing and validation of this utility must follow a more statistical procedure, in which threat estimates by the utility are compared to results from a large number of measured ocean wave time series, some with identified rogue waves and others without rogues. The surface elevation time series utilized here were recorded during early 2017 by multiple CDIP ocean buoys. Sample output from the prototype utility is provided in Section 4.1. Testing formats are described in Section 4.2, and test results are summarized in Section 4.3.

4.1 Sample Rogue Threat Utility Output

The prototype rogue threat index utility constructed for WW3, *ww3_rti.ftn*, presently produces gridded 0.25° lat-lon maps of the RTI and each causal factor for the world's oceans between approximately 50°N and 50°S latitude (e.g., Figure 13). These maps may be combined with H_s data on the same grid to identify rogue wave "hot spots", where a combination of larger H_s and large RTI indicates a higher likelihood of dangerously extreme waves (Figure 15).

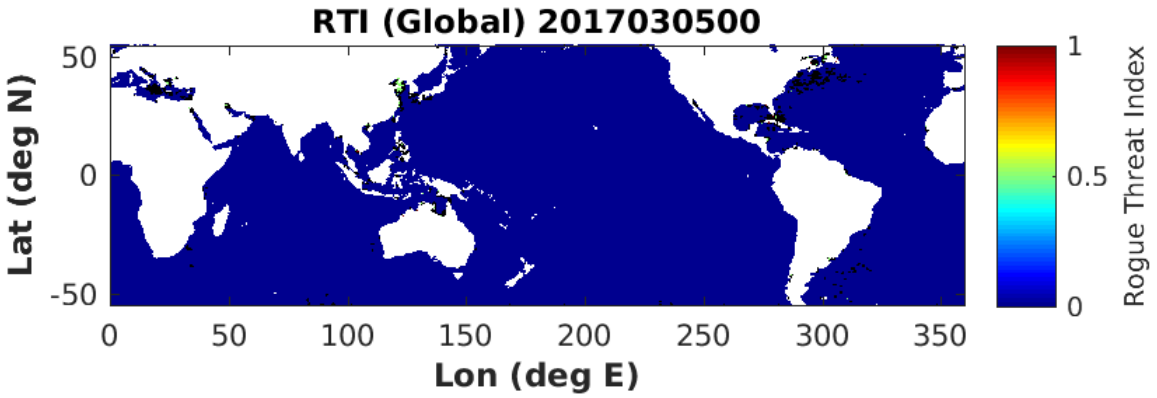

Figure 13. Sample of gridded global RTI output from rogue threat utility. As is normally expected, very few areas are highlighted as elevated threats. A close examination of the figure will reveal areas of moderate RTI near South Korea and in the Caribbean, among other locations.

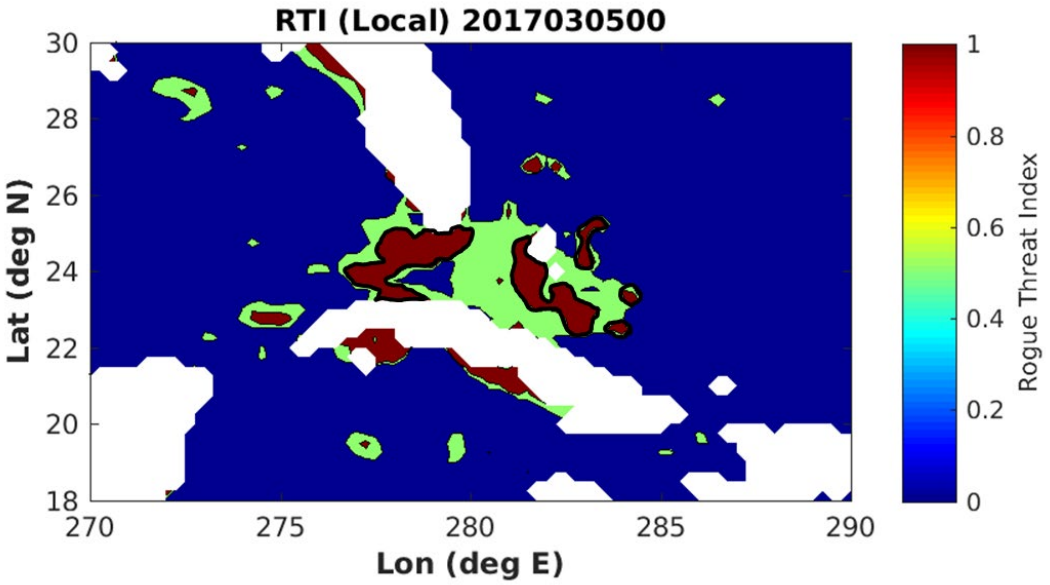

Figure 14. Zoomed view of RTI results from Figure 13, displaying elevated RTI in the Caribbean Sea between Florida and Cuba. Light green regions indicate mildly elevated threat, while dark red corresponds to higher rogue likelihood.

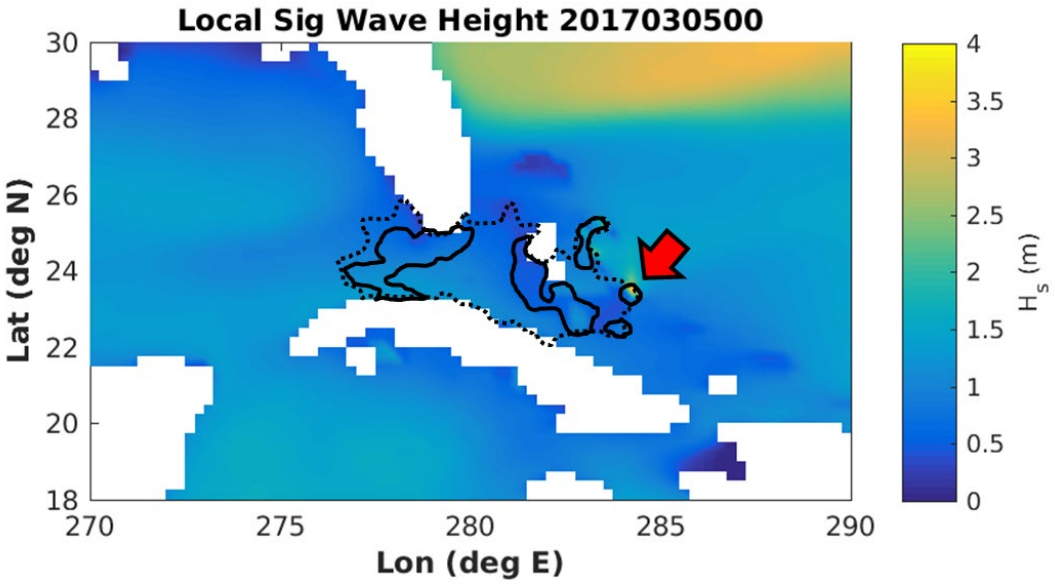

Figure 15. Significant wave height output from WW3 for same time and area as shown in Figure 14. Dashed black line marks boundaries of "mildly elevated" RTI region from that figure, while sold black outlines correspond to higher rogue likelihood regions. Large red arrow on this figure identifies a small region where large H_s and high RTI coincide. This will trigger an alert message from the rogue utility if anticipated rogue waves are larger than the maximum acceptable height, H_{max} , specified by system operator.

4.2 Test Configuration

Preliminary testing utilized rogue event data and other surface time series from CDIP buoys 029, 067, 071, 092, and 098 for the first three months of 2017, together with spectral restart files and binary current and wind field output files generated by WW3 at 3hr intervals.

The method of evaluation is to measure the correlation of positive/negative (i.e., rogue/non-rogue) results at the selected buoys with rogue threat estimates computed for corresponding time steps in WW3. The "positive" results are generated for the specific time and location of each identified rogue event that is detected at one of the five buoys. The RTI and its component values are computed from WW3 spectra together with local current and wind data at the time step and grid cell that are closest to each identified event. The "negative" results are generated by averaging RTI and components over the non-rogue period immediately preceding each event (these periods could be anywhere from 1 – 20 days long). Results are summarized below and in Figure 16.

4.3 Results

The preliminary goal of these tests is to achieve a measureable difference in mean RTI between the positive (rogue) and negative (non-rogue) cases, with clearly larger mean value of RTI in rogue cases. As illustrated in the figure, we did obtain a slightly larger mean value of RTI for positive cases, as well as larger mean values of C_{BFI} and C_{dir} ; however, the average of C_{curr} values was somewhat smaller for the positive cases than for the negative ones. C_w was FALSE for all cases examined in this preliminary test, so it is not displayed here.

Weighting of each causal factor in equation (22) can be used to increase or decrease the relative importance of each causal factor to the RTI. In this case, because the results for C_{BFI} and C_{dir} correctly favor the positive rogue events, increasing their weights in (22), in order to more greatly emphasize this signal in the RTI, might be appropriate. The question of factor weighting will be examined more fully in the upcoming calibration and validation tests of the rogue threat utility.

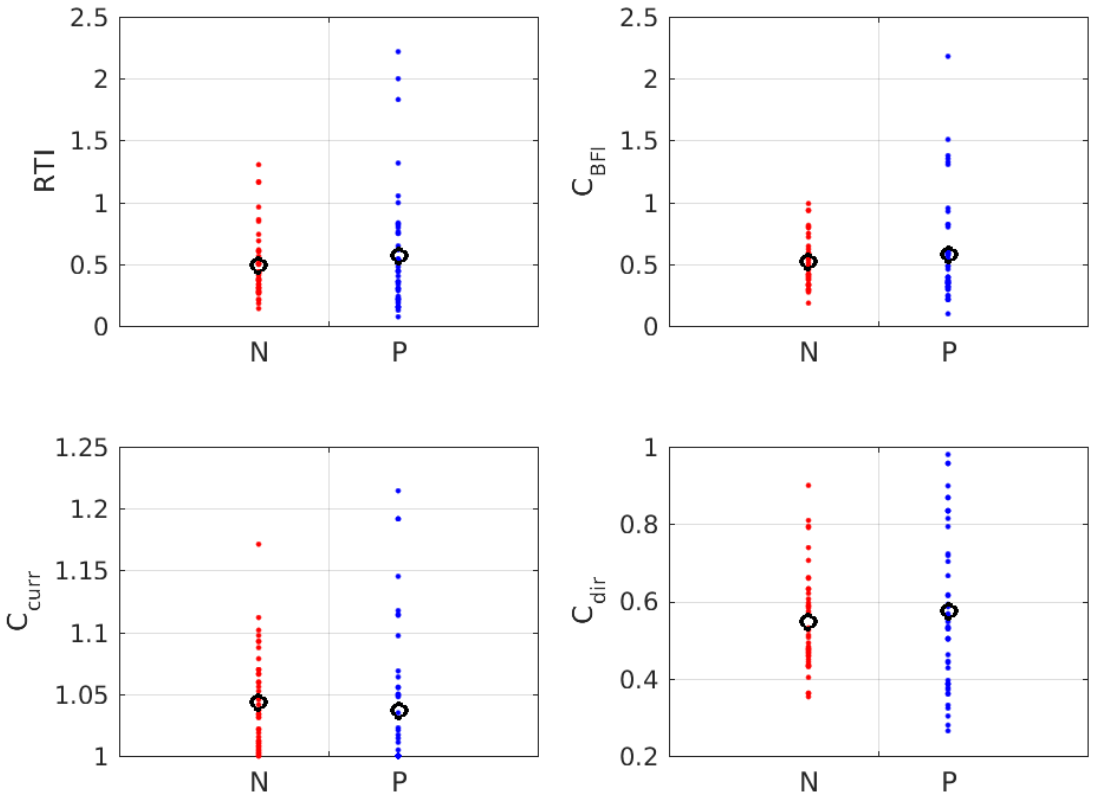

Figure 16. Results of preliminary tests of rogue threat index computation for both rogue (P) and non-rogue (N) conditions, as recorded a five selected CDIP buoys between Jan.-Mar. 2017. Red dots show mean values of RTI and its components for non-rogue periods. Blue dots show computed RTI and components for identified times and locations of rogue events. Black circles on each panel show average of all values. (Note that C_w was FALSE for all analyzed events, so it is not included here.)

5 CONCLUSIONS AND PLANS

As described above, we have developed a prototype WAVEWATCH III utility for the estimation of the relative likelihood of rogue waves, as a function of four primary environmental causal factors. The most fundamental of these factors is the modulational instability of the wave spectrum, generally evaluated with the Benjamin Feir Index (BFI). This tendency can be enhanced as a result of interactions between waves and adverse currents. In contrast, it can be reduced by specific variations in the wave directional distribution, or the effects of strong winds. We have used numerical modeling to validate and/or quantify the effects of each causal factor on the spectral modulation, combining the contributions to compute a single Rogue Threat Index (RTI). These computations have been implemented in the prototype utility, which presently requires some user interaction and configuration to generate results but will ultimately be

converted to a fully automated form. A full calibration and validation of the utility is expected to be completed within a 6.4 transition that will likely begin in mid-FY20 or early FY21.

The rogue threat index utility described here is intentionally limited in its scope and does not presently include all important environmental factors that either contribute to or dampen the growth of rogue waves through nonlinear modulation. The theory of rogue waves continues to advance, bringing improved understanding of causal factor mechanisms, identifying previously unknown causal factors, and clarifying the relative importance of each contributor to rogue development. As our understanding changes, the RTI estimator is expected to evolve and adopt new causal factors, modify computations of existing components, and adjust the relative weights given to each component.

5.1 Calibration and Validation

The causal factor components of the RTI will be subjected to a more extensive calibration in preparation for the 6.4 validation testing, using data from a 10-year range (2000-2009). Spectra, currents, and wind fields will be processed by the rogue threat utility at 34 buoy locations for all identified rogue events with wave height exceeding 2m (~2000 events), as well as for an equivalent number of time periods that did not include rogues. "Single rogue" evaluations will be conducted for all confirmed rogue events that were not accompanied by another confirmed event within ± 2 days. "Multi-rogue" evaluations will identify the time ranges during which more than one rogue wave event was recorded at a single buoy location with a separation of less than 2 days.[4] The mean and maximum RTI values for the entire period will be computed, and then these results will be plotted against the number of rogue events and correlated.

Computed values of RTI (for single time steps) and average RTI (across multiple time steps) will be plotted against rogue occurrences, seeking consistently high RTI values for confirmed rogue events. Causal factor weights will again be varied to investigate the importance of each contribution and improve RTI correlation. Planned metrics include the following:

a) For accumulated individual rogue/non-rogue tests, the mean minus standard deviation of RTI for all "Positive" (P) rogue events must exceed the mean plus standard deviation of RTI for all "Negative" (N) non-rogue events (or intervals); i.e.,

$$\overline{\boldsymbol{RTI}_P} - \sigma_{RTI,P} > \overline{\boldsymbol{RTI}_N} + \sigma_{RTI,N} \tag{23}$$

where σ is used to represent the standard deviation of all RTI values for either P or N results.

b) For multi-rogue-event tests, the correlation of time-averaged RTI values plotted against the number of rogue events will be at least $r^2 = 0.7$.

c) Additional metrics (e.g., spatially averaged RTI vs total events in a region) will be developed and applied as deemed appropriate.

Error estimates will be developed for the model-based sources of each causal factor and used to adjust the relative weighting of each factor in the RTI computation and optimize the fit of RTI

[4] Based on a cursory review of buoy data, it is anticipated that these cases may involve roughly two to five consecutive rogue events.

values to data. The relative importance of each causal factor in the RTI computation will be investigated for a range of environmental conditions and rogue wave magnitudes. Different operational products may require different calibration coefficients (e.g., RTI for single time steps, or average RTI over multi-day, multi-rogue periods). Uncertainty/error in wave, current, and wind model data will also be considered.

5.2 Future Plans

The RTI algorithm is designed with a simple, separable format, in order to facilitate modification of existing components or add representations of new factors. In addition to the four causal factors presently included in the index, we plan to develop and validate quantitative representations of modulation effects induced by bathymetry, mesoscale atmospheric turbulent storm eddies, and specific wave frequency distributions.

While it is well known that shallower bathymetry causes waves to shoal, steepen, and eventually break, it has also been shown to increase the likelihood of rogue wave development. Trulsen et al. (2012) provide experimental evidence that a sloping bathymetry can produce both a maximum of skewness and kurtosis concurrent with a local maximum of probability for a large wave envelope at the shallow end of the slope. They demonstrate this result for long-crested waves in a 2DH wave flume, and conclude that the probability of rogue waves will be greater under such conditions. Ducrozet and Gouin (2017) use an HOS model to extend this result to directionally spread, 3D waves. They note that, as in deep water, the occurrence of rogue waves is reduced for directionally broad sea states. The RTI utility is presently limited to deep water, but we would like to investigate and quantify the effects of bathymetry in a future system upgrade, should funding be obtained.

As noted earlier in this report, strong winds blowing in the same direction as that of highly nonlinear wave groups can dampen their modulation, blocking their development into rogue waves, while opposing winds appear to slow the breaking process and enable further rogue wave growth. A contrasting effect that enhances modulational instability is proposed by Pleskachevsky et al. (2012), who investigated strong wind gusts in moving mesoscale storm cells in the North Sea. Their measurements determined that the cell footprints sometimes produced a consistent system of increased wind velocity near the sea surface; the system itself was noted to propagate at roughly the speed of the local swell waves. Using spectral wave modeling, the authors estimated that a group of such cells moving with the swell could transfer a large amount of energy to the waves, leading to a local increase of significant wave height of more than 6m in 10-20 minutes. Although such mesoscale gusts are not presently captured by the resolution of operational forecasting models, they may be incorporated at a future date and/or assimilated from optical and radar satellite measurements. If such data become available, this effect could eventually also be added to the RTI formulation.

As described in the Introduction, Barbariol et al. (2017) have implemented a statistical approach to the estimation of space-time extreme waves in WAVEWATCH III, based on the Euler characteristics method outlined in Fedele (2012). This stochastic approach analytically determines the return period of space-time extremes in short-crested, stormy seas, based on the frequency-directional surface wave spectrum. As part of the evaluation and validation of the rogue threat utility, we intend to run a series of simulations comparing RTI estimates to the output of the Barbariol system for selected time and space domains in which rogue waves have

been measured. Ultimately, if deemed appropriate, the space-time extremes computation may also be incorporated into an expanded RTI estimate.

5.3 Dissemination of Code

WW3 is presently considered an open-source, "community" model. As mentioned earlier, the primary public-release version of the model is maintained in a Subversion repository at NOAA/NCEP, with a new user/developer interface provided via GitHub. At present, the code described in this report is not on the svn repository, but is instead on an NRL repository. Our intent is to transfer this utility (and associated test cases) to the GitHub trunk and ultimately onto the NOAA/NCEP repository after completion of the validation and transition process described at the beginning of Section 5. This is most likely to be completed by the end of FY23.

6 REFERENCES

Babanin, A., 2011: Change of regime of air-sea interactions in extreme weather conditions. *Proc. 20th Australasian Coastal and Ocean Eng. Conf.*, Perth, September 2011.

Babanin, A., and W.E. Rogers, 2014: Generation and limiters of rogue waves. *Int. J. Oc. Clim. Sys.* **5(2)**, 39-49.

Babanin, A., 2013: Physics-based approach to wave statistics and probability. *Proc. 32nd Int. Conf. on Ocean, Offshore and Arctic Eng. OMAE2013*, Nantes, France, July 2013.

Babanin, A., T. Waseda, T. Kinoshita, and A. Toffoli, 2011: Wave breaking in directional fields. *J. Phys. Oceanog*., **41**, 145-156.

Babanin, A., D. Chalikov, I. Young, and I. Savelyev, 2010: Numerical and laboratory investigation of breaking of steep two-dimensional waves in deep water. *J. Fluid Mech*., **644**: 433-463.

Babanin, A., and Y. Soloviev, 1998: Variability of directional spectra of wind-generated waves, studied by means of wave staff arrays. *Marine & Freshwater Res*., **49(2)**, 89-101.

Barbariol, F., J.H.G.M Alves, A. Benetazzo, F. Bergamasco, L. Bertotti, S. Carniel, L. Cavaleri, Y.Y. Chao, A. Chawla, A. Ricchi, M. Sclavo, and H. Tolman, 2017: Numerical modeling of space-time wave extremes using WAVEWATCH III. *Oc. Dynamics*, **67(3-4)**, 535-549.

Benetazzo, A., F. Barbariol, F. Bergamasco, A. Torsello, S. Carniel, and M. Sclavo, 2015: Observation of extreme sea waves in a space-time ensemble. *J. Phys. Oceanogr*., **45**, doi:10.1175/JPO-D-15-0017.1.

Benjamin, T. B., and J. E. Feir, 1967: The disintegration of wave trains on deep water. Part I. Theory, *J. Fluid Mech*., **27**, 417–430.

Bliven, L., N. Huang, and S. Long, 1986: Experimental study of the influence of wind on Benjamin-Feir sideband instability. *J. Fluid Mech*., **162**, 260-273.

Cavaleri, L., L. Bertotti, L. Torrisi, E. Bitner-Gregersen, M. Serio, and M. Onorato, 2012: Rogue waves in crossing seas: the Louis Majesty accident. *J. Geophys. Res*., **117**, 8pp.

Chabchoub, A., N.P. Hoffman, and N. Akhmediev, 2011: Rogue wave observation in a water wave tank. *Phys. Rev. Lett*., **106**, 204502.

Chalikov, D., 2009: Freak waves: their occurrence and probability. *Phys. Fluids* **21(7)**, doi:10.1063/1.3155713.

Chalikov, D., and A. Babanin, 2012: Simulation of breaking in spectral environment. *J. Phys. Oceanog*., **42**, 1745-1761.

Chen, G, Q. Xiong, P. Morris, E. Paterson, A. Sergeev, and Y.-C. Wang, 2014: OpenFOAM for computational fluid dynamics". *Notices of Amer. Math. Soc*. **61**(4), 354–363, doi:10.1090/noti1095.

Choi, W., 2009: Nonlinear surface waves interacting with a linear shear current. *Math. and Computers in Simul*. **80**, 29-36.

Ducrozet G., F. Bonnefoy, D. Le Touzé, and P. Ferrant, 2016: HOS-ocean: open-source solver for nonlinear waves in open ocean based on high-order spectral method. *Comp. Phys. Comm*. **203**, 245-254.

Ducrozet, G., and M. Gouin, 2017: Influence of varying bathymetry in rogue wave occurrence within unidirectional and directional sea-states. *J. Ocean Engrg and Marine Energy* **3**(4), 309-324.

Ellison, A., 1987: Effect of seed dimorphism on the density-dependent dynamics of experimental populations of Atriplex triangularis (Chenopodiaceae). *Amer. J. Botany*, **74**(8), 1280-1288.

Fedele, F., G. Gallego, A. Yezzi, A. Benetazzo, L. Cavaleri, M. Sclavo, and M. Bastianini, 2012: Euler characteristics of oceanic sea states. *Math. and Computers in Simulat*. **82**, 1102-1111.

Fedele, F., 2012: Space-time extremes in short-crested storm seas. *J. Phys. Oceanogr*., **42**, 1601-1614.

Galchenko, A., A. Babanin, D. Chalikov, I. Young, B. Haus, 2012: Influence of wind forcing on modulation and breaking of one-dimensional deep-water wave groups. *J. Phys. Oceanog*. **42**, pp. 928-939.

Goda, Y., 1970: Numerical experiments on wave statistics with spectral simulation. *Rep. Port Harb. Res. Inst.*, **9**, 57.

Gramstad, O., E. Bitner-Gregersen, K. Trulsen, and J. Borge, 2018: Modulational instability and rogue waves in crossing sea states. *J. Phys. Oceanog*., **48**, 1317-1331.

Hjelmervik, K.B., and K. Trulsen, 2009: Freak wave statistics on collinear currents. *J. Fluid Mech*. **637**, 267–284.

Janssen, P.A.E.M., 2003: Nonlinear four-wave interactions and freak waves. *J. Phys. Oceanogr*., **33**, 863–88.

Johnston, C., 2014: *Extreme wave statistics within the mouth of the Columbia River*. Master's Thesis, Naval Postgraduate School, Monterey, CA, Dec. 2014, *https://apps.dtic.mil/dtic/tr/fulltext/u2/a620915.pdf* .

Kharif, C., E. Pelinovsky, and A. Slunyaev, 2009: *Rogue Waves in the Ocean*. Springer: 216p.

Kharif, C. and E. Pelinovsky, 2003: Physical mechanisms of the rogue wave phenomenon. *Eur. J. Mech. B Fluids*, **22**, 603–634.

Lavrenov, I.V. 1998: The wave energy concentration at the Agulhas current off South Africa. *Nat. Hazards*, **17**, 117–127.

Liu, P., 2007: A chronology of freaque wave encounters. *Geofizika* **24(1)**, 57-70.

Ma, G., F. Shi, and J.T. Kirby, 2012: Shock-capturing non-hydrostatic model for fully dispersive surface wave processes. *Ocean Model*., **43–44**, 22–35.

Manolidis, M., M. Orzech, and J. Simeonov, 2019: Rogue wave formation on adverse current gradients. *J. Mar. Sci. & Engrg*. **7(26)**, 16pp.

Manzetti, S., 2018: Mathematical modeling of rogue waves: A survey of recent and emerging mathematical methods and solutions. *Axioms*, **7**, 42.

McLean, J., 1982: Instabilities of finite-amplitude water waves. *J. Fluid Mech*., **114**, 315-330.

Mori, N., M. Onorato, and P. Janssen, 2011: On the estimation of the kurtosis in directional sea states for freak wave forecasting. *J. Phys. Oceanog*., **41**: 1484-1497.

Onorato, M., D. Proment, and A. Toffoli, 2011: Triggering rogue waves in opposing currents. *Phys. Rev. Lett*., **107**, 184502.

Onorato, M., D. Proment, and A. Toffoli, 2010: Freak waves in crossing seas. *Eur. Phys. J. Special Topics* **185**, 45-55.

Onorato, M., et al., 2009: Statistical properties of mechanically generated surface gravity waves: A laboratory experiment in a 3D wave basin, *J. Fluid Mech*., **627**, 235–257.

Onorato, M., A.R. Osborne, M. Serio, and S. Bertone, 2001: Freak waves in random oceanic sea states. *Phys. Rev. Lett*., **86**, 5831.

Pleskachevsky, A.L., S. Lehner, and W. Rosenthal, 2012: Storm observations by remote sensing and influences of gustiness on ocean waves and on generation of rogue waves. *Ocean Dynamics*, **62**, 1335-1351.

Rogers, W.E., and G.P. van Vledder, 2013: Frequency width in predictions of windsea spectra and the role of the nonlinear solver. *Ocean Modelling*, **70**, 52–61.

Ruban, V.P., 2012: On the nonlinear Schrödinger equation for waves on a nonuniform current. *JETP Lett*., **95**, 486–491.

Toffoli, A., E. Bitner-Gregersen, A. Osborne, M. Serio, and J. Monbaliu, and M. Onorato, 2011: Extreme waves in random crossing seas: laboratory experiments and numerical simulations. *Geophys. Res. Ltr*., **38**, L06605.

Toffoli, A., A. Babanin, M. Onorato, and T. Waseda, 2010: Maximum steepness of oceanic waves: field and laboratory experiments. *Geophys. Res. Ltr*., **37**, L05603.

Tolman, H.L., 1991: A Third generation model for wind-waves on slowly varying, unsteady, and inhomogeneous depths and currents. *J. Phys. Oceanogr.* **21(6)**, 782-797.

Tolman, H.L., B. Balasubramaniyan, L.D. Burroughs, D.V. Chalikov, Y.Y. Chao, H.S. Chen, and V.M. Gerald, 2002: Development and implementation of wind-generated ocean surface wave models at NCEP. *Weather and Forecasting (NCEP Notes)*, **17**, 311-333.

Trulsen, K., and K. Dysthe, 1992: Action of windstress and breaking on the evolution of a wavetrain. *Proc. IUTAM Symposium*, Sydney, Australia, 244-249.

Trulsen, K., Zeng, H., and Gramstad, O., 2012: Laboratory evidence of freak waves provoked by non-uniform bathymetry. *Phys. of Fluids* **24**, doi:10.1063/1.4748346.

WAMDI Group, 1988. The WAM model--A third generation ocean wave prediction model. *J. Phys. Oceanogr.,* **18***,* 1775-1810.

Waseda, T., T. Kinoshita, and H. Tamura, 2009: Evolution of a random directional wave and freak wave occurrence. *J. Phys. Oceanog*., **39**, 621–639.

WAVEWATCH III® Development Group (WW3DG), 2019: User manual and system documentation of WAVEWATCH III® version 6.07. Tech. Note 333, NOAA/NWS/NCEP/MMAB, College Park, MD, USA, 320 pp. + Appendices.

Zakharov, V., 1968: Stability of periodic waves of finite amplitude on the surface of a deep fluid. *J. Appl. Mech. Tech. Phys*., **9**, 190–194.

Zakharov, V.E. 1967: The instability of waves in nonlinear dispersive media. *Sov. Phys.-JETP*, **24**, 737–744.

7 FURTHER READING

Adcock, T.A.A., and P.H. Taylor, 2014: The physics of anomalous ('rogue') ocean waves. *Rep. Prog. Phys.*, **77**, 105901.

Fedele, F., J. Brennan, S. Ponce de Leon, J. Dudley, and F. Bias, 2016: Real world ocean rogue waves explained without the modulational instability. *Nature Scientific Rpts*., **6**, 27715.

Fedele, F., and M.A. Tayfun, 2009: On nonlinear wave groups and crest statistics. *J. Fluid Mech*., 620, 221-239.

Fedele, F., 2008: Rogue waves in oceanic turbulence. *Physica D*, **237**, 2127-2131.

Hasselmann, K., 1966: Feynman diagrams and interaction rules of wave-wave scattering processes, *Rev. Geophys.*, **4**(1), 1–32, doi:10.1029/RG004i001p00001.

Komen, G. J., Cavaleri, L., Donelan, M., Hasselmann, K., Hasselmann, S., and P.A.E.M. Janssen, 1994. *Dynamics and Modelling of Ocean Waves.* Cambridge Univ. Press, 532 pp.